

# Three-dimensional magnetohydrodynamic simulation of the solar magnetic flux emergence

## Parametric study on the horizontal divergent flow

Shin Toriumi and Takaaki Yokoyama

Department of Earth and Planetary Science, University of Tokyo, 7-3-1 Hongo, Bunkyo-ku, Tokyo 113-0033, Japan  
e-mail: toriumi@eps.s.u-tokyo.ac.jp

Received / Accepted

### ABSTRACT

*Context.* Solar active regions are formed through the emergence of magnetic flux from the deeper convection zone. Recent satellite observations have shown that a horizontal divergent flow (HDF) stretches out over the solar surface just before the magnetic flux appearance.

*Aims.* The aims of this study are to investigate the driver of the HDF and to see the dependency of the HDF on the parameters of the magnetic flux in the convection zone.

*Methods.* We conduct three-dimensional magnetohydrodynamic (3D MHD) numerical simulations of the magnetic flux emergence and vary the parameters in the initial conditions. An analytical approach is also taken to explain the dependency.

*Results.* The horizontal gas pressure gradient is found to be the main driver of the HDF. The maximum HDF speed shows positive correlations with the field strength and twist intensity. The HDF duration has a weak relation with the twist, while it shows negative dependency on the field strength only in the case of the stronger field regime.

*Conclusions.* Parametric dependencies analyzed in this study may allow us to probe the structure of the subsurface magnetic flux by observing properties of the HDF.

## 1. Introduction

The dynamics of the rising magnetic flux and the formation process of solar active regions have widely been investigated through a series of analytical and numerical studies. Parker (1975) first calculated the rising speed of a flux tube in the convection zone (CZ) by considering a force balance between the magnetic buoyancy and the aerodynamic drag acting on the flux tube, while Schüssler (1979) simulated a buoyant emergence of a flux tube in the CZ in a two-dimensional (2D) scheme. Moreno-Insertis & Emonet (1996) and Emonet & Moreno-Insertis (1998) investigated the dependency of the rising tube on the initial twist intensity and found that the tube needs a certain degree of twist to hold its coherency. After Shibata et al. (1989) and Magara (2001) conducted 2D simulations of flux emergence from the surface layer into the corona, 3D simulations have been carried out by, among others, Fan (2001) and Archontis et al. (2004). Murray et al. (2006) simulated other 3D flux emergences of this kind and surveyed the tube's dependency on the initial field strength and twist intensity.

Recently, Toriumi & Yokoyama (2010, 2011, 2012) combined the CZ, the photosphere/chromosphere, and the corona into a single computational domain and simulated magnetic flux emergence from a deeper CZ both in 2D and 3D. As a result, the initial flux placed at a depth of  $-20$  Mm starts its emergence in the solar interior, which then slows down gradually in the uppermost CZ. This is because the plasma pushed up by the emerging flux rises to the isothermally-stratified (i.e. convectively-stable) surface layer and is then trapped and compressed between them,

which, in turn, suppresses the rising flux from below. Such compressed plasma will escape laterally around the photospheric layer from the rising flux as a horizontal divergent flow (HDF), just before the flux itself reaches the surface. Using SDO/HMI data, Toriumi et al. (2012) observed the emerging active region located away from the solar disk center and found the HDF in the Dopplergram, up to about 100 min before the start of the flux emergence.

In the present study, we report the results of the parametric survey of the 3D magnetohydrodynamic (MHD) flux emergence simulation. The aims of this study are to investigate which force drives the HDF and to observe the dependence of the HDF on the parameters in the simulation. One important feature of this HDF study is that it can be a probe for exploring the physical state of the magnetic field in the upper CZ. That is, we may be able to obtain valuable information on the subsurface layers from the direct optical observation at the surface. Therefore, in this numerical study, we vary the parameters of the initial flux tube, and then check the characteristics of the consequent HDF seen at the surface layer.

In the next section we introduce the basic setup of the numerical calculation. In Section 3 we show the results of the parametric survey, and in Section 4 we provide some analytic explanations of the results. We finally summarize the paper in Section 5.

## 2. Numerical Setup

The basic MHD equations, normalizing units, computational domain size, grid spacings, boundary conditions, and background

stratification are the same as those in Toriumi & Yokoyama (2012). The MHD equations in vector form are:

$$\frac{\partial \rho}{\partial t} + \nabla \cdot (\rho \mathbf{V}) = 0, \quad (1)$$

$$\frac{\partial}{\partial t}(\rho \mathbf{V}) + \nabla \cdot \left( \rho \mathbf{V} \mathbf{V} + p \mathbf{I} - \frac{\mathbf{B} \mathbf{B}}{4\pi} + \frac{\mathbf{B}^2}{8\pi} \mathbf{I} \right) - \rho \mathbf{g} = 0, \quad (2)$$

$$\frac{\partial \mathbf{B}}{\partial t} = \nabla \times (\mathbf{V} \times \mathbf{B}), \quad (3)$$

$$\begin{aligned} & \frac{\partial}{\partial t} \left( \rho U + \frac{1}{2} \rho \mathbf{V}^2 + \frac{\mathbf{B}^2}{8\pi} \right) \\ & + \nabla \cdot \left[ \left( \rho U + p + \frac{1}{2} \rho \mathbf{V}^2 \right) \mathbf{V} + \frac{c}{4\pi} \mathbf{E} \times \mathbf{B} \right] - \rho \mathbf{g} \cdot \mathbf{V} = 0, \end{aligned} \quad (4)$$

and

$$U = \frac{1}{\gamma - 1} \frac{p}{\rho}, \quad (5)$$

$$\mathbf{E} = -\frac{1}{c} \mathbf{V} \times \mathbf{B}, \quad (6)$$

$$p = \frac{k_B}{m} \rho T, \quad (7)$$

where  $\rho$  denotes the gas density,  $\mathbf{V}$  velocity vector,  $p$  pressure,  $\mathbf{B}$  magnetic field,  $c$  the speed of light,  $\mathbf{E}$  electric field, and  $T$  temperature, while  $U$  is the internal energy per unit mass,  $\mathbf{I}$  the unit tensor,  $k_B$  the Boltzmann constant,  $m (= \text{const.})$  the mean molecular mass, and  $\mathbf{g}$  the uniform gravitational acceleration. We assume the medium to be an inviscid perfect gas with a specific heat ratio  $\gamma = 5/3$ . All the physical values are normalized by the pressure scale height  $H_0 = 200$  km for length, the sound speed  $C_{s0} = 8$  km s<sup>-1</sup> for velocity,  $\tau_0 \equiv H_0/C_{s0} = 25$  s for time, and  $\rho_0 = 1.4 \times 10^{-7}$  g cm<sup>-3</sup> for density, all of which are the typical values in the photosphere. The units for pressure, temperature, and magnetic field strength are  $p_0 = 9.0 \times 10^4$  dyn cm<sup>-2</sup>,  $T_0 = 4000$  K, and  $B_0 = 300$  G, respectively.

Here, 3D Cartesian coordinates  $(x, y, z)$  are used, where  $z$  is parallel to the gravitational acceleration vector,  $\mathbf{g} = (0, 0, -g_0)$ , and  $g_0 = C_{s0}^2/(\gamma H_0)$  by definition. The simulation domain is  $(-400, -200, -200) \leq (x/H_0, y/H_0, z/H_0) \leq (400, 200, 250)$ , resolved by  $1602 \times 256 \times 1024$  grids. In the  $x$ -direction, the mesh size is  $\Delta x/H_0 = 0.5$  (uniform). In the  $y$ -direction ( $z$ -direction), the mesh size is  $\Delta y/H_0 = 0.5$  ( $\Delta z/H_0 = 0.2$ ) in the central area of the domain, which gradually increases for each direction. We assume periodic boundaries for both horizontal directions and symmetric boundaries for the vertical direction.

The background atmosphere consists of three different layers. From the bottom, the layers are the adiabatically stratified CZ, the cool isothermal photosphere/chromosphere, and the hot isothermal corona. The stratification in the CZ ( $z/H_0 < 0$ ) is given as

$$T = T_{\text{ph}} - z \left| \frac{dT}{dz} \right|_{\text{ad}}, \quad (8)$$

where  $T_{\text{ph}}/T_0 = 1$  is the respective temperature in the photosphere/chromosphere and

$$\left| \frac{dT}{dz} \right|_{\text{ad}} = \frac{\gamma - 1}{\gamma} \frac{mg_0}{k_B} \quad (9)$$

**Table 1.** Summary of the simulation cases

Case <sup>a</sup>	Field strength $B_{\text{tube}}/B_0$	Twist $qH_0$	Wavelength $\lambda/H_0$
A	67	0.1	400
B	133	0.1	400
C	33	0.1	400
D	67	0.2	400
E	67	0.05	400
F	67	0.1	100
G	67	0.1	25

**Notes.** <sup>(a)</sup> Case A is the same as that simulated in Toriumi & Yokoyama (2012). Cases B and C are for different field strengths than that of case A, while D and E are for different twists, and F and G different wavelengths.

is the adiabatic temperature gradient. The profile above the surface is

$$T(z) = T_{\text{ph}} + \frac{1}{2}(T_{\text{cor}} - T_{\text{ph}}) \left\{ \tanh \left[ \frac{z - z_{\text{cor}}}{w_{\text{tr}}} \right] + 1 \right\}, \quad (10)$$

where  $T_{\text{cor}}/T_0 = 100$  is the temperatures in the corona,  $z_{\text{cor}}/H_0 = 10$  is the base of the corona, and  $w_{\text{tr}}/H_0 = 0.5$  is the transition scale length. Based on the temperature distribution above, the pressure and density profiles are defined by the equation of static pressure balance:

$$\frac{dp(z)}{dz} + \rho(z)g_0 = 0. \quad (11)$$

The initial flux tube is embedded in the CZ at  $z_{\text{tube}}/H_0 = -100$ , i.e.,  $z_{\text{tube}} = -20$  Mm, of which the axial and azimuthal profiles are given as

$$\begin{cases} B_x(r) = B_{\text{tube}} \exp \left( -\frac{r^2}{R_{\text{tube}}^2} \right), \\ B_\phi(r) = qr B_x(r) \end{cases}, \quad (12)$$

respectively, where  $B_{\text{tube}}$  is the axial field strength,  $r$  the radial distance from the tube's center ( $y_{\text{tube}}/H_0, z_{\text{tube}}/H_0 = (0, -100)$ ),  $R_{\text{tube}}$  the typical radial size, and  $q$  the twist intensity. For the pressure balance between the field and the plasma, the pressure distribution inside the tube is defined as  $p_i = p(z) + \delta p_{\text{exc}}$  (the subscript "i" denotes inside the tube), where the pressure excess  $\delta p_{\text{exc}} (< 0)$  is described as

$$\delta p_{\text{exc}} = \frac{B_x^2(r)}{8\pi} \left[ q^2 \left( \frac{R_{\text{tube}}^2}{2} - r^2 \right) - 1 \right]. \quad (13)$$

The density inside the tube is also defined as  $\rho_i = \rho(z) + \delta \rho_{\text{exc}}$ , where

$$\delta \rho_{\text{exc}} = \rho(z) \frac{\delta p_{\text{exc}}}{p(z)} \exp \left( -\frac{x^2}{\lambda^2} \right), \quad (14)$$

and  $\lambda$  is the perturbation wavelength. That is, the middle of the tube,  $x/H_0 = 0$ , is in thermal equilibrium with external media and is most buoyant. The buoyancy decreases as  $|x|/H_0$  increases.

The parameters we varied are the field strength  $B_{\text{tube}}$ , the twist  $q$ , and the perturbation wavelength  $\lambda$ . Table 1 summarizes the cases in this study. The case simulated in Toriumi & Yokoyama (2012) is named here as case A, while cases B–F are for different field strength, twist, and wavelength than those of A. Here we fixed the tube's radial size at  $R_{\text{tube}}/H_0 = 5$  for all the cases. It should be noted that the critical twist for the kink instability is  $qH_0 = 0.2$  (Linton et al. 1996). Therefore, all the tubes examined here are stable or, at least, marginally stable against the instability at the beginning of the calculation.

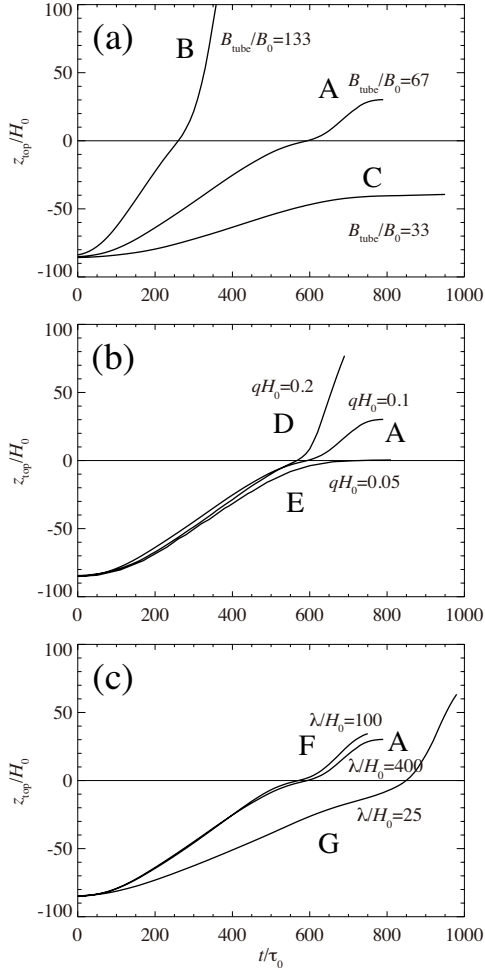


**Fig. 1.** Height-time evolution of the flux tube. (a) Cases for different  $B_{\text{tube}}$ . (b) Cases for different  $q$ . (c) Cases for different  $\lambda$ .

### 3. Simulation Results

#### 3.1. General Evolution

Fig. 1 shows the temporal evolution of the apex of the rising tube,  $z_{\text{top}}(t)$ . Also, in Fig. 2, we plot the total field strength,  $\log_{10}(|B|/B_0)$ , of the initial condition for case A and the final states for all the cases. As can be seen in Fig. 1a, it is clear that the tubes with stronger field  $B_{\text{tube}}$  rise faster. The rising speed of each tube in the CZ is in simple proportion to the initial field strength, which is well in accordance with Murray et al. (2006) and other previous studies. Case A, which has a middle field strength, shows deceleration just before it reaches the surface. This deceleration is the result of the plasma accumulation, which is caused by the trapping of material between the rising tube and the isothermally-stratified photosphere above the tube. After a while, the tube then starts further emergence into the atmosphere (see the top panels in Fig. 2). As for the strongest case in B, the accumulation becomes less marked, and thus the tube almost directly passes through the surface layer and expands into the higher corona, without undergoing strong deceleration (Fig. 2B). When the field is very weak, as in case C, the tube stops its emergence halfway to the surface, since the tube's buoyancy is not strong enough to continue its emergence (Fig. 2C).

Fig. 1b shows the evolution with different twist  $q$ . In this figure, all three tubes are seen to rise almost at the same rate in the CZ, which is again consistent with previous studies (e.g.

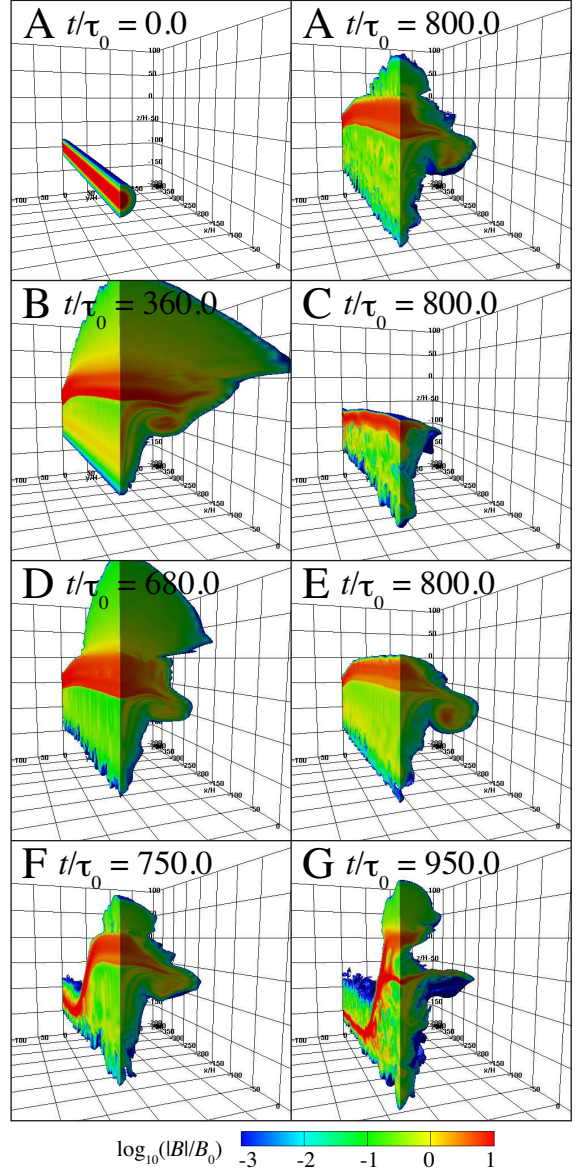


**Fig. 2.** Total magnetic field strength of the initial condition for case A and the final states for cases A to G, plotted over the range  $-400 \leq x/H_0 \leq 0$  and  $0 \leq y/H_0 \leq 200$ .

Murray et al. 2006). When the twist is weak and thus cannot hold the coherency (case E), the tube expands and suffers deformation by aerodynamic drag. As a result, the tube cannot maintain a strong enough magnetic field to continue its further emergence (Fig. 2E).

Fig. 1c compares three cases with different wavelengths of the initial perturbation. The initial wavelength is crucial for two factors: the curvature force (magnetic tension), which pulls down the rising tube, and the drainage of the internal media due to gravity, which encourages the emergence. When the wavelength is smaller, the curvature force is expected to be stronger, while the drainage becomes more effective. In Fig. 1c the rising velocities of cases A and F are almost the same, which indicates that both effects cancel each other out. However, the shortest wavelength tube (case G) shows a much slower emergence rate in the CZ, which indicates that the curvature force is more effective and slows down the emergence. As for the emergence above the surface layer, on the contrary, Fig. 1c shows an exactly op-

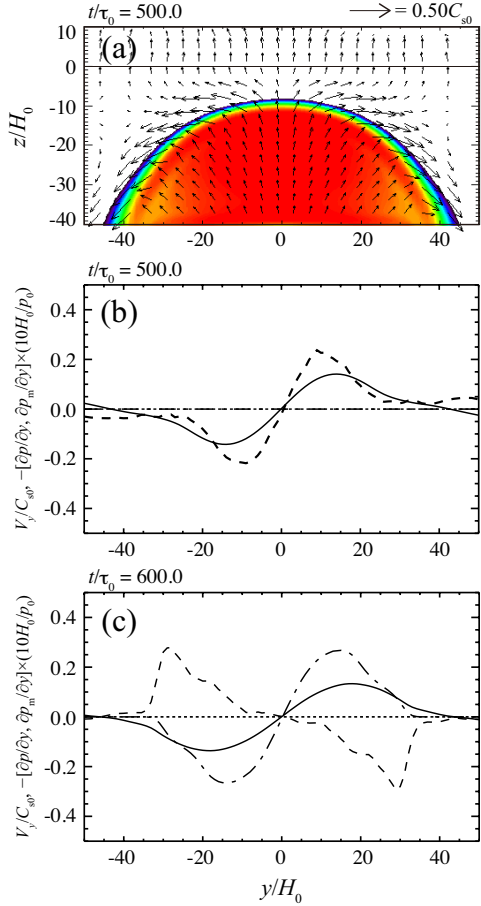


**Fig. 3.** (a) Cross-sectional profile of the rising magnetic flux tube (case A). Plotted value is the logarithmic field strength  $\log_{10}(|B|/B_0)$  averaged over  $6.5 \leq x/H_0 \leq 13.5$ , at the time  $t/\tau_0 = 500$ . The color saturates at  $|B|/B_0 = 1.0$  (red) and  $-4.0$  (purple). (b) Horizontal velocity  $V_y/C_{s0}$  (thick solid), pressure gradient  $-\partial p/\partial y \times (10H_0/p_0)$  (dashed), and magnetic pressure gradient  $-\partial p_m/\partial y \times (10H_0/p_0)$  (dash-dotted), at  $t/\tau_0 = 500$ . (c) Same as (b) but for  $t/\tau_0 = 600$ .

posite trend that the rising is much faster when the wavelength is shortest (case G). One may find that, in Fig 2G, the main tube remains in the CZ at around  $z/H_0 = -50$ , while the upper part has been detached from the main tube and has started further emergence into the atmosphere. The reason for the rapid ascent may be because, in the shortest wavelength case, namely, in the highly curved loops, the draining of the plasma from the apex is more effective, which helps the faster emergence above the photosphere.

### 3.2. Driver of the HDF

Fig. 3a is the cross-sectional distribution of the field strength of Case A. The plotted value is the logarithmic field strength  $\log_{10}(|B|/B_0)$  averaged over  $6.5 \leq x/H_0 \leq 13.5$ , i.e., around  $x/H_0 = 10$ . The reason we choose this  $x$ -range is to select one folded structure at the tube’s surface (see Fig. 3 of Toriumi & Yokoyama 2012). In this figure, there is a flow field in front of the rising flux tube, which is flowing from the apex to the flanks of the tube. One characteristic of this plasma layer is the horizontal divergent flow (HDF) that is seen at the solar surface just before the flux tube itself emerges.

To investigate which force drives the HDF, in Figs. 3b and c, we plot the horizontal flow velocity  $V_y$ , pressure gradient  $-\partial p/\partial y$ , and magnetic pressure gradient  $-\partial p_m/\partial y$ , averaged over  $6.5 \leq x/H_0 \leq 13.5$  and  $-10 \leq z/H_0 \leq 0$ , where  $p_m = B^2/(8\pi)$ . Magnetic tension is not plotted here, since it is rather small compared to the two other forces. At  $t/\tau_0 = 500$ , before the tube reaches the uppermost CZ,  $z/H_0 > -10$ , the horizontal flow is clearly driven only by the gas pressure, and, of course, the magnetic pressure gradient is zero. Therefore, we can conclude that the HDF prior to the flux appearance is caused by the pressure gradient. This is consistent with other numerical simulations including thermal convection (Cheung et al. 2010). At  $t/\tau_0 = 600$ , the shallow layer is covered by the rising tube and the gas pressure gradient reverses its sign. Instead, the magnetic pressure gradient becomes dominant enough to drive the flow.

### 3.3. Dependence of the HDF

In this subsection, we show the dependence of the HDF on the initial field strength  $B_{\text{tube}}$  and on the twist  $q$ . The investigated parameters are the duration of the HDF (from the HDF start to flux appearance),  $\Delta t/\tau_0$ , and the maximum HDF velocity,  $\max(V_y)/C_{s0}$ , during this time period. Here we defined the start time of the HDF as “when the horizontal speed  $V_y$  in the horizontal range  $-50 \leq y/H_0 \leq 50$ , averaged over  $6.5 \leq x/H_0 \leq 13.5$  and  $-10 \leq z/H_0 \leq 0$ , exceeds  $0.06C_s (= 0.5 \text{ km s}^{-1})$ ” and the flux appearance as “when the field strength  $|B|$  in this range exceeds  $0.67B_0 (= 200 \text{ G})$ .”

Figs. 4a and b show the dependence of the duration on the field strength  $B_{\text{tube}}$  and the twist  $q$ . Panel (a) is the comparison among the different field strength cases. A comparison of cases A and B, the middle and stronger field tubes, shows that the time duration is longer for the stronger field. If other stronger cases are considered (here we also plot two stronger tube cases other than A, B, and C), however, it may be found that the duration decreases with field strength. Thus, we can divide these cases into two groups: stronger cases that show a decreasing trend, which is fitted by a function of  $B_{\text{tube}}^{-1}$ , and a middle case that deviates from the decreasing trend. The weakest tube, case C, did not reach the surface. That is why the duration is 0 for case C. In contrast, in Panel (b), the duration is almost constant for the different twist cases.

Dependence of the maximum HDF speed,  $\max(V_y)$ , is shown in Figs. 4c and d. Panel (c) indicates the positive linear correlation with the field strength  $B_{\text{tube}}$ . Again, the speed of case B is plotted as zero, since it did not reach the surface. Note that, in Panel (a), we found a gap between the middle-field regime and the stronger-field regime. Thus the linear fitting in Panel (c) might not reflect the actual trend. Nevertheless, the maximum speed basically increases with field strength. In Panel (d), we can see that the maximum HDF velocity is clearly proportional to the initial twist  $q$ .

## 4. Analytic Explanation

In this section, the dependencies of the rising speed and of the HDF on the physical parameters obtained in Section 3 are analytically explained.

### 4.1. Rising Speed

In Section 3.1, we found that the rising speed of the flux tube is proportional to the field strength  $B_{\text{tube}}$  and the dependence on the

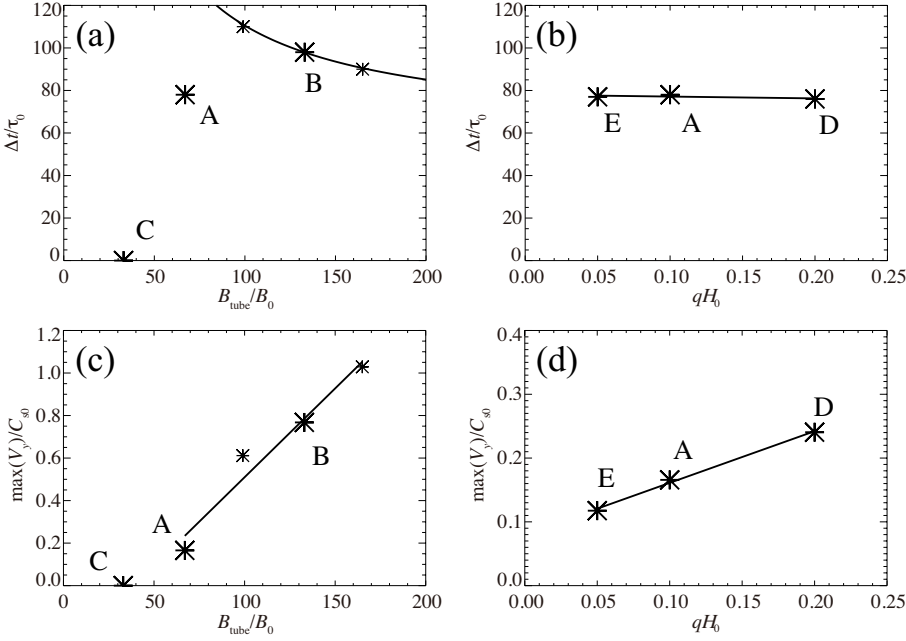


**Fig. 4.** (a) Dependence of the HDF duration  $\Delta t$  on the field strength  $B_{\text{tube}}$ , and (b) that on the twist  $q$ . (c) Dependence of the maximum HDF speed  $\max(V_y)$  on the field strength  $B_{\text{tube}}$ , and (d) that on the twist  $q$ . In Panel (a) and (c) we also plot other field strength cases, which are indicated by smaller asterisks. Solid lines are the fitted curves; (a)  $\Delta t/\tau_0 = 5.08 \times 10^3/(B_{\text{tube}}/B_0) + 5.97 \times 10$ , (b)  $\Delta t/\tau_0 = -8.57 \times (qH_0) + 7.80 \times 10$ , (c)  $\max(V_y)/C_{s0} = 8.35 \times 10^{-3} \times (B_{\text{tube}}/B_0) - 3.26 \times 10^{-1}$ , (d)  $\max(V_y)/C_{s0} = 8.10 \times 10^{-1} \times (qH_0) + 8.02 \times 10^{-2}$ .

twist  $q$  is significantly small. The curvature is effective for the flux tube with the shortest wavelength  $\lambda$ . Here we assume that the rising speed in the CZ is given as a terminal velocity where the buoyancy of the tube equals the aerodynamic drag by the surrounding flow field (Parker 1975; Moreno-Insertis & Emonet 1996) and the downward magnetic tension. Buoyancy, dynamic drag, and tension force acting on a unit cross-sectional area are written as

$$f_B = \frac{B^2}{8\pi H_p}, \quad (15)$$

$$f_D = C_D \frac{\rho V_z^2}{\pi R_{\text{tube}}}, \quad (16)$$

and

$$f_T = \frac{B^2}{4\pi R_c}, \quad (17)$$

respectively, where  $H_p = H_0(T/T_0)$  denotes the local pressure scale height,  $V_z$  the tube's vertical speed,  $C_D$  the drag coefficient of order unity, and  $R_c$  is the radius of curvature. The mechanical balance  $f_B = f_D + f_T$  yields the terminal velocity

$$V_\infty^2 = \frac{R_{\text{tube}} B^2}{4C_D \rho} \left( \frac{1}{2H_p} - \frac{1}{R_c} \right). \quad (18)$$

First, let us discuss the curvature effect. In Equation (18), the tension force is negligible for  $R_c \rightarrow \infty$ , while the tension becomes effective when  $R_c \sim 2H_p$ . The relationship between the curvature radius  $R_c$  and the perturbation wavelength  $\lambda$  is illustrated as Fig. 5a. Here, we write the tube's height as  $\Delta z = z_{\text{top}}(t) - z_{\text{tube}}$ . From this figure, we have

$$\begin{cases} R_c - R_c \cos \theta = \Delta z \\ R_c \sin \theta = \lambda \end{cases}, \quad (19)$$

which gives

$$\lambda = \sqrt{2R_c \Delta z - (\Delta z)^2}. \quad (20)$$

Thus, using the condition  $R_c \sim 2H_p$ , we obtain the critical wavelength for the tension to be effective:

$$\lambda_c = \sqrt{4H_p \Delta z - (\Delta z)^2}. \quad (21)$$

For instance, when the tube is halfway to the surface, i.e.,  $z_{\text{top}}/H_0 = -50$  and thus  $\Delta z/H_0 = 50$ , the local pressure scale height at this depth is  $H_p/H_0 \sim 21$ . Therefore, the critical wavelength is evaluated to be  $\lambda_c \sim 41.2H_0$ , and the flux tube with a wavelength smaller than this value will be resisted by the tension force,  $\lambda \lesssim \lambda_c \sim 41.2H_0$ . In Fig. 1c, we found that only the tube with  $\lambda = 25H_0$  shows slower emergence due to the effective curvature force, which satisfies the condition  $\lambda \lesssim \lambda_c$ .

Next, let us go on to the dependencies on the field strength and the twist, by considering  $R_c \rightarrow \infty$ . Now the equation of the terminal velocity (18) reduces to

$$\begin{aligned} V_\infty &= \sqrt{\frac{R_{\text{tube}}}{8C_D H_p \rho}} B_{\text{tube}} \sqrt{1 + q^2 r^2} \exp\left(-\frac{r^2}{R_{\text{tube}}^2}\right) \\ &\sim \sqrt{\frac{e^{-2} R_{\text{tube}}}{8C_D H_p \rho}} B_{\text{tube}} \sqrt{1 + q^2 R_{\text{tube}}^2}. \end{aligned} \quad (22)$$

Here, in the first line we use Equation (12) and in the second line we assume  $r \sim R_{\text{tube}}$ . From this equation, we see that the rising velocity is in simple proportion to the initial field strength  $B_{\text{tube}}$  when  $q$  is constant. If we change  $q$  with considering  $R_{\text{tube}} = 5H_0$ , for  $qH_0 = [0.05, 0.1, 0.2]$ , the third term in the right-hand-side of Equation (22) gives

$$\sqrt{1 + q^2 R_{\text{tube}}^2} = \begin{cases} 1.03 \\ 1.12 \\ 1.4 \end{cases}. \quad (23)$$

That is, the second term has only a weak positive correlation to the value of  $q$ . Therefore, the rising velocity of the flux tube is proportional to the field strength, while it is almost independent on the initial twist. The trend of the rising speed found in Section 3.1 is thus explained.



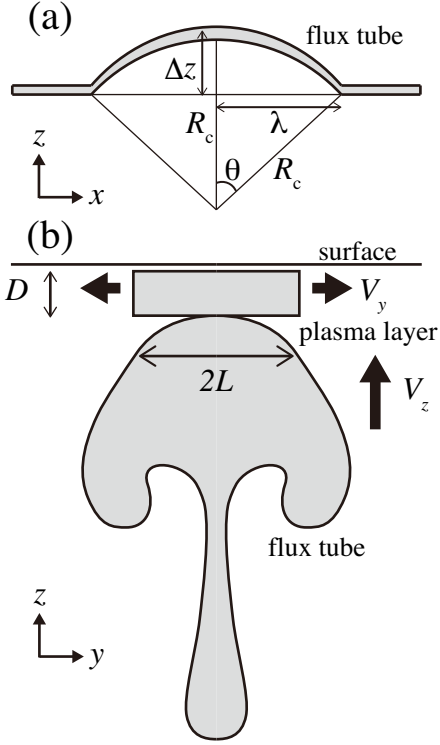


**Fig. 5.** (a) Cross-section of the rising flux tube along the axis (in the  $x - z$  plane). (b) Cross-section of the rising flux tube and the plasma layer ahead of the tube (in the  $y - z$  plane).

Note here that, if we substitute  $H_p \sim 40H_0$ ,  $\rho \sim 275\rho_0$  (values at  $z_{\text{tube}}$ ),  $B_{\text{tube}} = 67B_0$ ,  $q = 0.1/H_0$ , and  $R_{\text{tube}} = 5H_0$  (values for case A) and assume  $C_D \sim 1$  in Equation (22), we obtain  $V_\infty = 0.21C_{s0}$ , which is comparable to the simulation result  $\sim 0.17C_{s0}$  (Fig. 1). This agreement indicates that Equation (22) is a rather reasonable estimation of the tube's rising speed (see also Parker 1975; Moreno-Insertis & Emonet 1996).

#### 4.2. Dependence on the Twist

We found in Section 3.3 that when the twist  $q$  is varied while the field strength  $B_{\text{tube}}$  is kept constant, the duration of the HDF  $\Delta t$  is almost constant while the maximum horizontal speed  $\max(V_y)$  is proportional to  $q$ .

This feature can be explained by considering a simple model illustrated as Fig. 5b. Here the flux tube with a head size of  $2L$  is rising at  $V_z$ , which pushes the plasma layer with a thickness  $D$ . The thickness  $D$  is also described as  $D \sim |z_{\text{top}}(t)|$ , where  $z_{\text{top}}(t) = z_{\text{tube}} + \int_0^t V_z(t') dt'$ . From the discussion in Section 4.1,  $V_z$  and thus  $D$  are independent of  $q$ , which indicates that the HDF duration  $\Delta t \simeq D/V_z$  is also independent of  $q$ .

If we write the outflow speed as  $V_y$ , mass flux conservation can be written as

$$V_y = \frac{V_z}{D} L. \quad (24)$$

Here,  $V_z/D$  is independent of  $q$ . The head size of the tube  $L$ , however, depends on the twist  $q$ , since the aerodynamic drag peels away the tube's outer flux and its amount depends on the twist. The head size remains larger with  $q$ , which results in the stronger HDF;  $V_y \propto L(q)$ . Thus the maximum speed,  $\max(V_y)$ , will also depend on  $q$ .

It should be noted here that  $L$  and  $q$  are not always linearly correlated. According to Moreno-Insertis & Emonet (1996), the boundary of the expanded tube is well defined by the equipartition surface, where the kinetic energy density equals the magnetic energy density of the azimuthal field:

$$\frac{1}{2}\rho V^2 = \frac{B_\phi^2}{8\pi}. \quad (25)$$

On the basis of an analogy from Equation (12), the profile of the expanded tube at the equipartition surface, where the radial distance is  $r_1$  (the subscript "1" indicates the expanded tube), is assumed to be written as

$$\begin{cases} B_x(r_1) = B_{\text{tube1}} \exp\left(-\frac{r_1^2}{R_{\text{tube1}}^2}\right), \\ B_\phi(r_1) = qr_1 B_x(r_1) \end{cases}, \quad (26)$$

where  $B_{\text{tube1}}$  and  $R_{\text{tube1}}$  are the axial field and the typical radius, respectively. Then, Equation (25) reduces to

$$\frac{r_1}{R_{\text{tube1}}} \exp\left(-\frac{r_1^2}{R_{\text{tube1}}^2}\right) = \left(\frac{4\pi\rho V^2}{B_{\text{tube1}}^2}\right)^{1/2} \frac{1}{qR_{\text{tube1}}}. \quad (27)$$

Here we assume that  $V$  is more or less approximate to  $V_z$  and thus  $V$  does not depend on  $q$ . Other values of  $B_{\text{tube1}}$ ,  $R_{\text{tube1}}$ , and  $\rho$  are also assumed to be constant for different  $q$ . Here we introduce the notation  $\mu \equiv r_1/R_{\text{tube1}}$ . Then Equation (27) reduces to

$$\mu \exp(-\mu^2) = 1/\hat{q}, \quad (28)$$

or,

$$\mu^2 - \ln \mu = \ln \hat{q}, \quad (29)$$

where  $\hat{q} \equiv qR_{\text{tube1}}[B_{\text{tube1}}^2/(4\pi\rho V^2)]^{1/2}$ . For a larger radial distance,  $r_1 \gg R_{\text{tube1}}$ , i.e.,  $\mu \gg 1$ ,

$$\mu^2 \sim \ln \hat{q}. \quad (30)$$

Then we obtain

$$r_1 \sim R_{\text{tube1}} \left[ \ln(qR_{\text{tube1}}) + \frac{1}{2} \ln\left(\frac{B_{\text{tube1}}^2}{4\pi\rho V^2}\right) \right]^{1/2}. \quad (31)$$

Therefore, the effective size of the expanded tube  $L \sim r_1$  is at least positively correlated to  $q$ , but not in a linear manner.

#### 4.3. Dependence on the Field Strength

When the field strength at the tube's axis  $B_{\text{tube}}$  is varied while the twist  $q$  is fixed, the maximum HDF speed,  $\max(V_y)$ , is found to be roughly proportional to the field strength. From Equation (24), if we assume  $L/D$  is constant, the horizontal speed  $V_y$  and thus the maximum speed  $\max(V_y)$  are proportional to the field strength  $B_{\text{tube}}$ .

As for the HDF duration  $\Delta t$ , however, Fig. 4a clearly shows two regimes: stronger field cases that show a decreasing trend, and a middle case that deviates from this trend. Thus we should take into account the difference between these regimes.

First, let us focus on the stronger field regime. Since the rising speed is proportional to the field strength, stronger tubes emerge faster. In this case, the accumulated plasma ahead of the tube does not drain down so much because of the short emergence period, and thus the thickness of the plasma layer becomes almost the same for these cases. That is, the thickness of the layer

$D$  is constant and is independent of the rising speed  $V_z$ . Since the rising speed is proportional to the field strength  $B_{\text{tube}}$ , we have

$$\Delta t \simeq D/V_z \propto 1/B_{\text{tube}}. \quad (32)$$

Hence, the HDF duration is inversely proportional to the field strength, which explains the trend in the stronger field regime of the fitted inverse function in Fig. 4a.

As for the middle strength case, the emergence takes longer and thus the drainage of the accumulated plasma becomes more effective, resulting in the much thinner layer  $D$  compared to the rising speed  $V_z$ . Therefore, the HDF duration  $\Delta t \simeq D/V_z$  becomes shorter and thus deviates from the inverse trend in the stronger field cases.

## 5. Summary

In this parametric survey, we vary the axial field strength, twist, and perturbation wavelength of the initial flux tube. As a result, we found the following features.

The rising speed in the CZ strongly depends on the initial field strength but its correlation with the twist is weak. The emergence is resisted by the curvature force only in the case when the perturbation wavelength is shortest. According to the analytic study, the rising rate (terminal velocity) is written as  $V_\infty \propto B_{\text{tube}} \sqrt{1 + q^2 R_{\text{tube}}^2}$ , which indicates a strong dependence on the field strength and a weak correlation with the twist.

As the flux tube approaches the surface, the accumulated plasma ahead of the tube escapes horizontally around the surface layer, which is called the HDF. The driver of the HDF is found to be the pressure gradient.

When the field strength increases, the maximum HDF speed becomes higher, because the rising speed mainly depends on the field strength. The HDF duration is divided into two groups. For the stronger tube regime ( $B_{\text{tube}} \gtrsim 100B_0$ ), the duration is in simple inverse proportion to the field strength, while the weaker field regime ( $B_{\text{tube}} \lesssim 100B_0$ ) deviates from the trend in the stronger tube regime because the fluid draining is more effective.

The duration of the HDF is found to have no relation with the tube's twist, since the rising speed is independent of the twist. However, the maximum HDF speed shows a positive correlation with the twist. This feature is explained by considering the head size of the main tube that remains after the aerodynamic drag peels away the tube's outer field. The head size remains larger with the twist, which results in the stronger HDF.

If we apply the above dependencies of the HDF to the actual observations, we may be able to obtain information on the magnetic field in the subsurface layer, which we cannot observe optically.

*Acknowledgements.* The authors would like to thank the anonymous referee for improving the paper. S.T. is supported by Grant-in-Aid for JSPS Fellows. Numerical computations were carried out on NEC SX-9 and Cray XT4 at the Center for Computational Astrophysics, CfCA, of the National Astronomical Observatory of Japan. We are grateful to the GCOE program instructors of the University of Tokyo for proofreading/editing assistance.

## References

- Archontis, V., Moreno-Insertis, F., Galsgaard, K., Hood, A., & O'Shea, E. 2004, *A&A*, 426, 1047  
 Cheung, M. C. M., Rempel, M., Title, A. M., & Schüssler, M. 2010, *ApJ*, 720, 233  
 Emonet, T. & Moreno-Insertis, F. 1998, *ApJ*, 492, 804  
 Fan, Y. 2001, *ApJ*, 554, L111  
 Linton, M. G., Longcope, D. W., & Fisher, G. H. 1996, *ApJ*, 469, 954

- Magara, T. 2001, *ApJ*, 549, 608  
 Moreno-Insertis, F. & Emonet, T. 1996, *ApJ*, 472, L53  
 Murray, M. J., Hood, A. W., Moreno-Insertis, F., Galsgaard, K., & Archontis, V. 2006, *A&A*, 460, 909  
 Parker, E. N. 1975, *ApJ*, 198, 205  
 Schüssler, M. 1979, *A&A*, 71, 79  
 Shibata, K., Tajima, T., Steinolfson, R. S., & Matsumoto, R. 1989, *ApJ*, 345, 584  
 Toriumi, S., Hayashi, K., & Yokoyama, T. 2012, *ApJ*, 751, 154  
 Toriumi, S. & Yokoyama, T. 2010, *ApJ*, 714, 505  
 Toriumi, S. & Yokoyama, T. 2011, *ApJ*, 735, 126  
 Toriumi, S. & Yokoyama, T. 2012, *A&A*, 539, A22